Available online at www.sciencedirect.com

ScienceDirect

journal homepage: www.elsevier.com/locate/he

Investigation of praseodymium and samarium co-doped ceria as an anode catalyst for DIR-SOFC fueled by biogas

B. Bochentyn [a,*], P. Błaszczak [a], M. Gazda [a], A. Fuerte [b], S.-F. Wang [c], P. Jasiński [d]

[a] Advanced Materials Center, Faculty of Applied Physics and Mathematics, Gdansk University of Technology, 80-233 Gdańsk, ul. Narutowicza 11/12, Poland

[b] Energy Department, Centre for Energy, Environment and Technology (CIEMAT), Av. Complutense 40, Madrid, 28040, Spain

[c] Department of Material and Mineral Resources Engineering, National Taipei University of Technology, 1, Sec. 3, Zhongxiao E. Rd., Taipei, 106, Taiwan

[d] Advanced Materials Center, Faculty of Electronics, Telecommunications and Informatics, Gdansk University of Technology, 80-233 Gdańsk, ul. Narutowicza 11/12, Poland

HIGHLIGHTS

- Pr and Sm co-doped ceria synthesized by reverse microemulsion method.
- Composition of outlet gases analyzed by Fourier Transformed Infrared Spectroscopy.
- $Ce_{0.9}Sm_{0.1}O_{2-\delta}$ and $Ce_{0.8}Pr_{0.05}Sm_{0.15}O_{2-\delta}$ - attractive catalysts for DIR- SOFC.

GRAPHICAL ABSTRACT

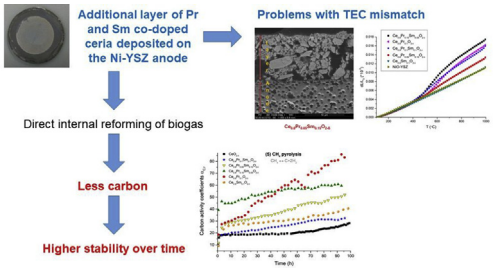

ARTICLE INFO

Article history:
Received 2 March 2020
Received in revised form
15 July 2020
Accepted 16 July 2020
Available online 18 August 2020

Keywords:
Biogas reforming
Direct internal reforming
Carbon deposition

ABSTRACT

The Pr and Sm co-doped ceria (with up to 20 mol.% of dopants) compounds were examined as catalytic layers on the surface of SOFC anode directly fed by biogas to increase a lifetime and the efficiency of commercially available DIR-SOFC without the usage of an external reformer.

The XRD, SEM and EDX methods were used to investigate the structural properties and the composition of fabricated materials. Furthermore, the electrical properties of SOFCs with catalytic layers deposited on the Ni-YSZ anode were examined by a current density-time and current density-voltage dependence measurements in hydrogen (24 h) and biogas (90 h). Composition of the outlet gasses was in situ analysed by the FTIR-based unit.

It has been found out that $Ce_{0.9}Sm_{0.1}O_{2-\delta}$ and $Ce_{0.8}Pr_{0.05}Sm_{0.15}O_{2-\delta}$ catalytic layers show the highest stability over time and thus are the most attractive candidates as catalytic

* Corresponding author.
E-mail address: beata.bochentyn@pg.edu.pl (B. Bochentyn).

https://doi.org/10.1016/j.ijhydene.2020.07.146

SOFC
FTIR

materials, in comparison with other investigated lanthanide-doped ceria, enhancing direct internal reforming of biogas in SOFCs.

Introduction

Ceria-based compounds are very attractive materials for electrochemical applications, such as solid oxide fuel cells (either electrolyte or anode [1,2]), oxygen storage materials [3], oxygen sensors or catalysts of partial oxidation of hydrocarbons [4,5]. They present high mobility of oxygen ions [3], high oxygen storage capacity (OSC) [3], attractive redox catalytic properties [1–5], chemical compatibility with water and carbon dioxide at high temperatures [4] and sufficient resistance to reduction under relatively low oxygen partial pressures [4]. The high oxygen mobility in ceria promotes the mechanism of carbon removal, which in turn, should contribute to the stability of the catalysts on hydrocarbon conversion reactions [3].

Undoped ceria (CeO_2) has a fluorite-type structure with 8-fold coordination of cations. In reductive atmospheres the oxygen vacancies are compensated by the reduction of Ce^{4+} to Ce^{3+}. As a result, n-type electronic conduction through small polaron thermally activated hopping occurs [4,6]. To introduce the oxygen vacancies and to increase the ionic conductivity of these compounds, cerium atoms in the structure can be substituted with some aliovalent cations. Among them one can find e.g., Gd^{3+} or Sm^{3+} [7,8]. Another interesting type of dopant is praseodymium [9,10], which shows a significant redox activity under reductive conditions. At reduced pO_2 Pr acts in a similar manner to Gd or Sm. It is a fixed valent dopant non prone to changes in the oxygen vacancy concentration with temperature [9,10]. At high pO_2 the concentration of oxygen vacancies becomes strongly dependent on temperature and oxygen partial pressure [9,10].

In order to obtain a ceria-based compound with a considerable concentration of oxygen vacancies, the strategy of aliovalent co-doping of ceria with Gd and Pr has been suggested in the literature [9]. In this case oxygen non-stoichiometry is formed as a result of charge compensation. Another pair of dopants, Nd and Sm, led to improved electrical conductivity thanks to the lowering of an association enthalpy of the oxygen vacancy and the dopant ions [11–13]. Other factors, which may play a role in co-doping effect are: raise of a configurational entropy, modification of an elastic strain in the crystal lattice and changes in the grain boundary composition [11–13].

In this paper, aliovalent co-doping procedure by Sm and Pr has been suggested. Then oxygen vacancies should be formed to compensate effectively negatively charged Sm^{3+}, Pr^{3+} and Ce^{3+} that partially substitute Ce^{4+}. Assuming ideal behaviour for the reduction of Pr and Ce in the lattice (invariant values of reaction entropies and enthalpies) the expected defect reactions leading to a formation of oxygen vacancies can be described by the following reactions [9]:

$$Sm_2O_3 \xrightarrow{CeO_2} 2Sm'_{Ce} + V_O^{\cdot\cdot} + 3O_O^x \quad (1)$$

$$2Pr_{Ce}^x + O_O^x \leftrightarrow 2Pr'_{Ce} + V_O^{\cdot\cdot} + \frac{1}{2}O_2(g) \quad (2)$$

$$2Ce_{Ce}^x + O_O^x \rightarrow 2Ce'_{Ce} + V_O^{\cdot\cdot} + \frac{1}{2}O_2(g) \quad (3)$$

where O_O^x is the oxide ion in its lattice site, $V_O^{\cdot\cdot}$ is an oxygen vacancy, Sm'_{Ce} is Sm^{3+} ion in Ce^{4+} ion site, Pr_{Ce}^x and Pr'_{Ce} are Pr^{4+} and Pr^{3+} ions in Ce^{4+} site, respectively.

It is clear from the above equations that both dopants lead to a formation of oxygen vacancies, which may have a positive effect on the partial oxidation of hydrocarbons catalysed with the use of these compounds. Therefore, in this work various nanocrystalline compounds of Pr and Sm co-doped ceria (with up to 20 mol.% of dopants) were fabricated by the reverse microemulsion synthesis method. Next, they were deposited in the form of layers on the surface of SOFC anode in aim to act as electrochemically active materials for the biogas reforming process. The aim of such a SOFC anode modification was to investigate the influence of these functional layers on a lifetime and efficiency of the commercially available solid oxide fuel cell operating under biogas without the need of an external reformer.

Experimental

The following compositions: $CeO_{2-\delta}$, $Ce_{0.9}Sm_{0.1}O_{2-\delta}$, $Ce_{0.9}Pr_{0.1}O_{2-\delta}$, $Ce_{0.8}Pr_{0.15}Sm_{0.05}O_{2-\delta}$, $Ce_{0.8}Pr_{0.1}Sm_{0.1}O_{2-\delta}$ and $Ce_{0.8}Pr_{0.05}Sm_{0.15}O_{2-\delta}$ have been fabricated via a reverse microemulsion method. A detailed description of the applied procedure is reported elsewhere [14].

The phase composition of the investigated materials was analysed using the X-ray diffraction method (XRD) by an X'Pert Pro MPD Philips diffractometer with Cu Kα (1.542 Å) radiation at room temperature. The size of crystallites was estimated based on the Scherrer formula: $C = k\lambda/[(B_e - B_t)\cos\theta]$, where C is an average diameter of the crystalline grain, k is a constant (assumed to be 0.9), λ is the X-ray wavelength, θ is the diffraction angle, B_e is the measured width of a peak profile and B_t is the instrumental width of a peak. The XRD patterns were also analysed by the Rietveld refinement method using a HighScore Plus software with the pseudo-Voigt profile function applied. As a starting point of the analysis, crystal structure parameters of CeO_2 (Fm-3m space group) were used [15]. The morphology of fabricated materials was examined using the FEI Quanta FEG 250 Scanning Electron Microscope (SEM). The thermal expansion coefficient of doped-ceria pellets (previously sintered at 1000 °C for 2 h) was determined

using the Netzsch DIL 402 PC dilatometer operating in 100–1000 °C temperature range under nitrogen atmosphere with 3 °C/min heating/cooling rate.

To form pastes, the obtained powders were ground in a mortar for about 1 h with ESL 403 organic binder (Electro-Science Laboratory, USA). The prepared pastes were deposited on the anode surface of a traditional 1-inch Solid Oxide Fuel Cell (Ni-YSZ anode, YSZ electrolyte and LSM-YSZ cathode). The catalytic layer was a circle of 16 mm diameter and 30 μm thickness. Finally, the modified fuel cells with deposited catalytic layers were fired at 1000 °C for 2 h.

Such prepared fuel cells were mounted in a measurement rig [16]. They were heated up to 800 °C with argon delivered to the anode side and then, to reduce nickel oxide, humidified hydrogen (3% H_2O) was supplied at 800 °C for 30 min and further at 750 °C for 20 h. After this time the hydrogen was replaced by wet synthetic biogas (3% H_2O) consisting of methane and carbon dioxide mixed at a volume ratio of 60:40. The total flow rate of the inlet gas mixture was 21 $cm^3\ min^{-1}$, ensuring constant gas supply to the FTIR system at the outlet of the fuel cell. This study was focused more on the comparison of the activity of additional catalytic layers and its influence on degradation rate, disregarding the optimal fuel utilisation factor discussed in other papers [17,18]. Two types of electrical measurements were collected during fuel cell operation in biogas: a current density versus voltage and a current density versus time at 0.65 V for the 90 h at 750 °C. A scheme representing a general procedure of the experiment applied in this work is shown in Fig. 1.

Simultaneously with electrical tests, an analysis of the composition of the outlet gases from SOFC was performed using a Fourier Transformed Infrared Spectroscopy (PerkinElmer Spectrum 100 with ZnSe optical windows). FTIR spectra were collected every 10 min within the wavenumber range of 4000–500 cm^{-1} with a resolution of 4 cm^{-1}. Concentrations of methane, carbon dioxide and carbon monoxide were then calculated. Although H_2 gas is not visible in FTIR spectra, after a calibration process, we were able to determine its concentration as a difference from 100% of summed CH_4, CO_2 and CO concentrations. Such an approach is correct and in line with expectations. Moreover, the conversion rates of CH_4 and CO_2 as well as the yields of H_2 and CO were calculated. A detailed description of the measuring system and analysis methods was reported elsewhere [16].

Results and discussion

Before operation in biogas

The XRD patterns of Ce(Pr,Sm)$O_{2-\delta}$ powders fabricated by a reverse microemulsion method are presented in Fig. 2. All

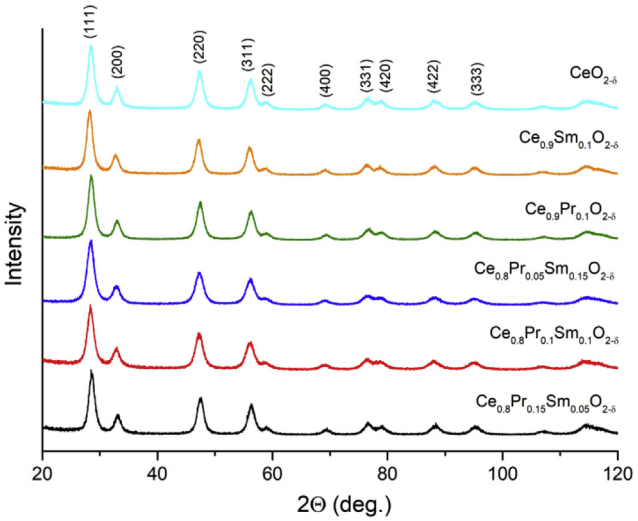

Fig. 2 – XRD patterns of Ce(Pr,Sm)$O_{2-\delta}$ powders fabricated by a reverse microemulsion method.

diffraction peaks can be attributed to $CeO_{2-\delta}$, which indicates that all materials are single-phase. Therefore it can be stated that the amount of dopants applied in this work (20 mol%) is below the solubility limit of Pr and Sm in ceria, what is in agreement with literature reports [19]. The obtained XRD data also allowed to estimate the size of the crystallites in the fabricated compounds. The results of the analysis are shown in Table 1. It can be found that all of the materials are nanocrystalline and that addition of dopant reduces the average size of crystallites (from ca. 10 to 7 nm). The unit cell parameters of analysed compounds both with the goodness of fit (GOF) values for Rietveld refinement are also presented in Table 1. The lowest lattice parameter was found for pure $CeO_{2-\delta}$ and $Ce_{0.9}Pr_{0.1}O_{2-\delta}$, because Ce^{4+} and Pr^{4+} ions have the smallest and comparable ionic radii, as shown in Table 1. However, when both Pr and Sm dopants were introduced into ceria, then there is no linear dependence between lattice parameter and the amount of dopant, what suggests that praseodymium exists in mixed-valence state ($^{3+}/^{4+}$) in these compounds [4,9].

The morphology of fabricated powders examined using Scanning Electron Microscopy is shown in Fig. 3. All doped-ceria compounds have similar, uniform microstructure with round-shape grains of an average size of 20 nm. The only exception is pure $CeO_{2-\delta}$ in which two types of grain shape are visible: round and flakes-like. The former has an average size of 20 nm and the latter up to 100 nm.

In the next step the chemical compatibility of the fabricated compounds with the NiO-YSZ anode material was investigated. For this purpose the powders of the doped ceria materials were mixed with NiO-YSZ powder at 50 vol% ratio,

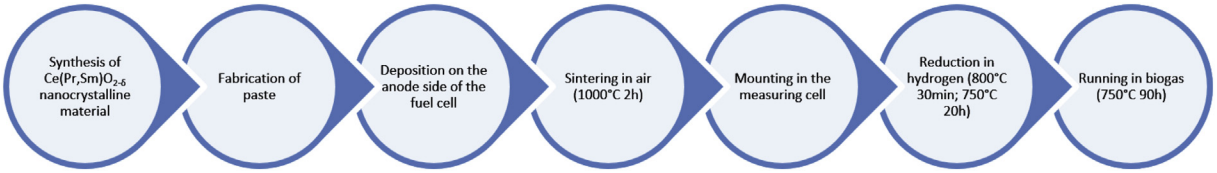

Fig. 1 – Procedure of the experiment.

Table 1 – Unit cell parameters, average size of crystallites (from XRD) and average size of grains (from SEM) calculated for the $Ce(Pr,Sm)O_{2-\delta}$ powders. Also the ionic radii for ions with coordination number equal 8 are shown.

Compound	Unit cell parameter, a (Å)	Size of crystallites, d_c (nm)	Size of grains, d_g (nm)	Ionic radius, R (Å) [20]
$CeO_{2-\delta}$	5.414 (GOF 1.56)	10.1 ± 0.4	20 up to 100	Ce^{3+} (1.143)
$Ce_{0.9}Sm_{0.1}O_{2-\delta}$	5.421 (GOF 2.57)	6.7 ± 0.6	21 ± 5	Ce^{4+} (0.97)
$Ce_{0.9}Pr_{0.1}O_{2-\delta}$	5.414 (GOF 2.04)	7.0 ± 0.3	20 ± 4	Sm^{3+} (1.079)
$Ce_{0.8}Pr_{0.15}Sm_{0.05}O_{2-\delta}$	5.420 (GOF 1.59)	6.2 ± 0.9	23 ± 3	Pr^{3+} (1.126)
$Ce_{0.8}Pr_{0.1}Sm_{0.1}O_{2-\delta}$	5.426 (GOF 2.07)	6.5 ± 0.3	25 ± 4	Pr^{4+} (0.96)
$Ce_{0.8}Pr_{0.05}Sm_{0.15}O_{2-\delta}$	5.426 (GOF 2.04)	6.2 ± 0.5	20 ± 3	

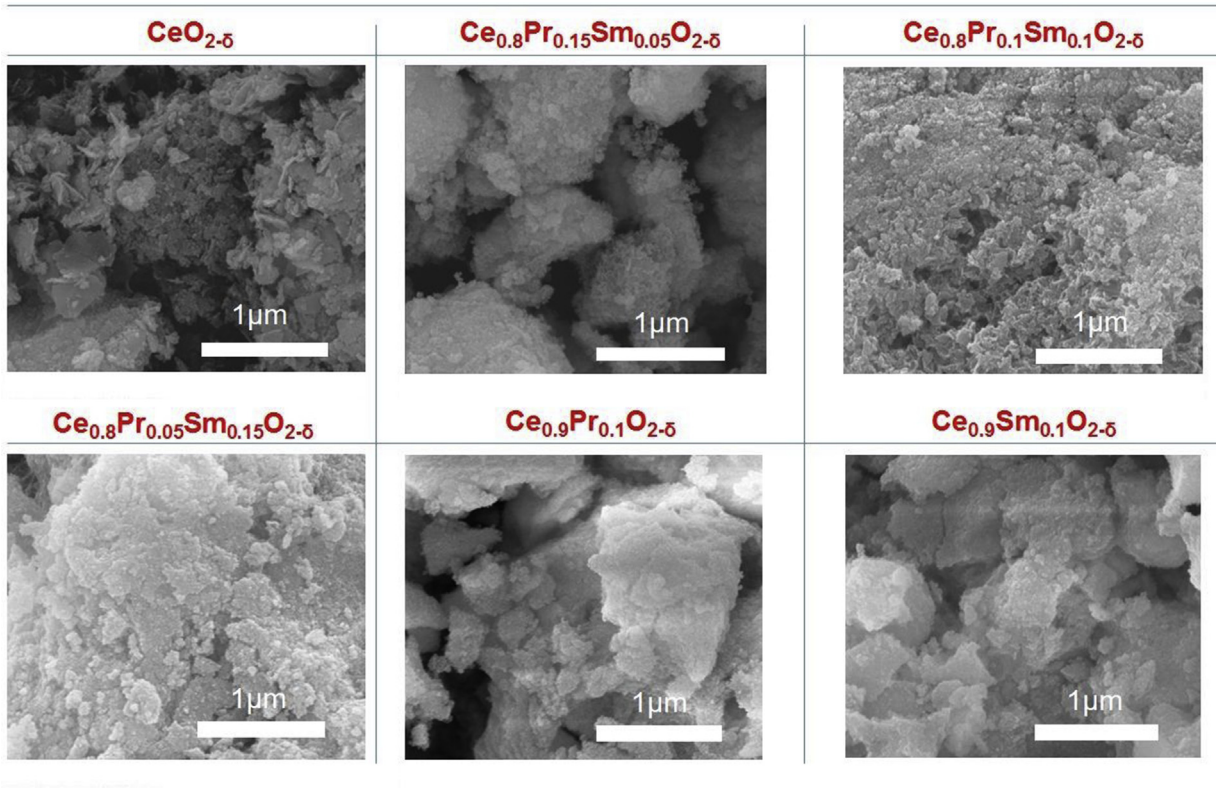

Fig. 3 – SEM images of $Ce(Pr,Sm)O_{2-\delta}$ powders fabricated by a reverse microemulsion method.

ground in an agate mortar, uniaxially pressed into pellets and subsequently sintered at 1000, 1100 and 1200 °C for 2 h. Then the XRD analysis was performed. In Fig. 4, a part of XRD pattern of $Ce_{0.8}Pr_{0.1}Sm_{0.1}O_{2-\delta}$ –NiO/YSZ composite after sintering at different temperatures for 2 h is shown. It is representative also of other compositions. It clearly indicates that at temperature above 1000 °C a chemical reaction between ceria and YSZ phase takes place. As a result, the secondary phase of $Ce_{0.33}Zr_{0.67}O_{2-\delta}$ is formed. This observation allows us to conclude that catalytic layers of ceria deposited on the surface of NiO-YSZ anode should be sintered at temperature not higher than 1000 °C to prevent the zirconium diffusion. Nevertheless, a potentially negative effect of the existence of this additional Ce–Zr–O phase depends on the part of the fuel cell in which it is formed [21–27]. For example, it was reported by Patel et al. [24] that when this phase occurs at the Ni/YSZ/CeO_2 anode operating with direct hydrocarbon feeds, it plays a key role in suppressing carbon formation and associated cell cracking. When Ciementi et al. [25] used $Zr_{0.35}Ce_{0.65}O_{2-\delta}$ to decorate the Ni-YSZ anode operating in methanol fuel, they also found that the addition of this compound not only enhanced the coking resistance due to its oxygen storage capability, but also increased the activity of the anode for fuel electro-oxidation due to the increased conductivity, as well as it affected the type of carbon that was formed [26]. On the other hand, if this phase forms also at the anode-electrolyte interface, then it will deteriorate the ionic conductivity of the thin YSZ electrolyte, lowering the performance of a whole fuel cell [27].

In the next stage of the experiment the doped-ceria powders were mixed with an organic binder to the form of a paste and deposited on the surface of NiO-YSZ fresh anode. Then they were sintered at 1000 °C for 2 h in the air. The cross sections of these samples were analysed by SEM to examine the quality of the interface between the ceria catalytic layer and the anodic support. Exemplary SEM images of $Ce_{0.9}Sm_{0.1}O_{2-\delta}$ and $Ce_{0.8}Pr_{0.05}Sm_{0.15}O_{2-\delta}$ interfaces are shown in Fig. 5. They are representative of two groups of compounds:

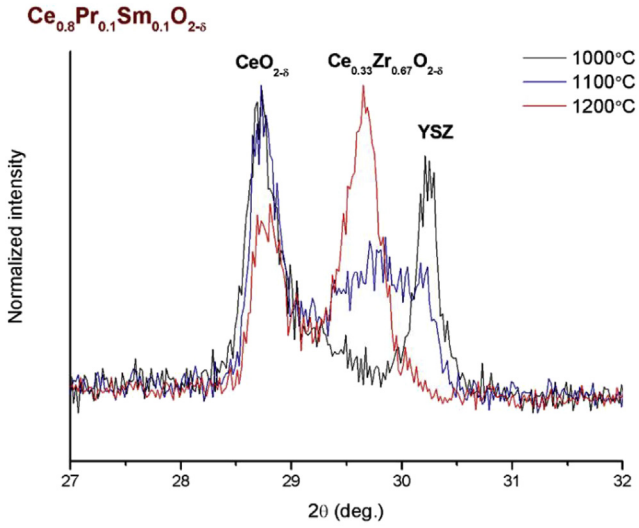

Fig. 4 – XRD patterns of $Ce_{0.8}Pr_{0.1}Sm_{0.1}O_{2-\delta}$ –NiO-YSZ composite after sintering at different temperatures for 2 h.

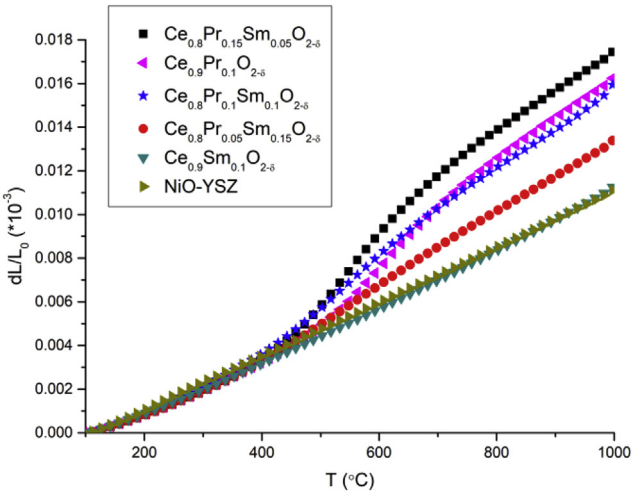

Fig. 6 – Expansion characteristics of fabricated compounds measured in N_2 atmosphere.

without and with praseodymium dopant. Catalytic layers without Pr have quite uniform microstructure, both in the case of grain size and porosity. In the interface with the anode support there are no visible cracks and no traces of delamination. When Pr is used as a dopant then the quality of the layer is quite poor. Large agglomerates, non-uniform porosity as well as a poor adhesion to the support are visible.

To better understand the source of this phenomenon the dilatometry studies of fabricated doped-ceria materials were performed. For reference also the NiO-YSZ anode was examined. The results are presented in Fig. 6. The calculated values of the expansion coefficient in defined temperature ranges are shown in Table 2. The thermal expansion coefficient of NiO-YSZ is equal to 12.4×10^{-6} K^{-1} and is in agreement with literature reports [28]. Among presented compounds only $Ce_{0.9}Sm_{0.1}O_{2-\delta}$ fits well to NiO-YSZ anode (TEC = 12.6×10^{-6} K^{-1}). This observation explains a very good quality of the interface between the $Ce_{0.9}Sm_{0.1}O_{2-\delta}$ catalytic layer and the anode support. It can also be noticed that all Pr-doped ceria samples show linear expansion below 400 °C. The expansion coefficients measured in this temperature range are close to that of NiO-YSZ. However, the dilatometry curves display a non-linear behaviour with an inflection point at ~550 °C. This deviation from linearity increases with increasing Pr content. Such behaviour has been previously

Table 2 – Values of total (thermal and chemical) expansion coefficients measured for fabricated compounds in different temperature ranges.

	α_{tot} (*10^{-6} K^{-1})		
	100-400 (°C)	400-700 (°C)	700-1000 (°C)
$Ce_{0.8}Pr_{0.15}Sm_{0.05}O_{2-\delta}$	11.1	32.1	18.6
$Ce_{0.8}Pr_{0.1}Sm_{0.1}O_{2-\delta}$	13.0	23.9	18.0
$Ce_{0.8}Pr_{0.05}Sm_{0.15}O_{2-\delta}$	10.4	17.7	16.2
$Ce_{0.9}Pr_{0.1}O_{2-\delta}$	11.8	27.9	19.2
$Ce_{0.9}Sm_{0.1}O_{2-\delta}$	12.6	12.6	12.6
NiO-YSZ	12.4	12.4	12.4

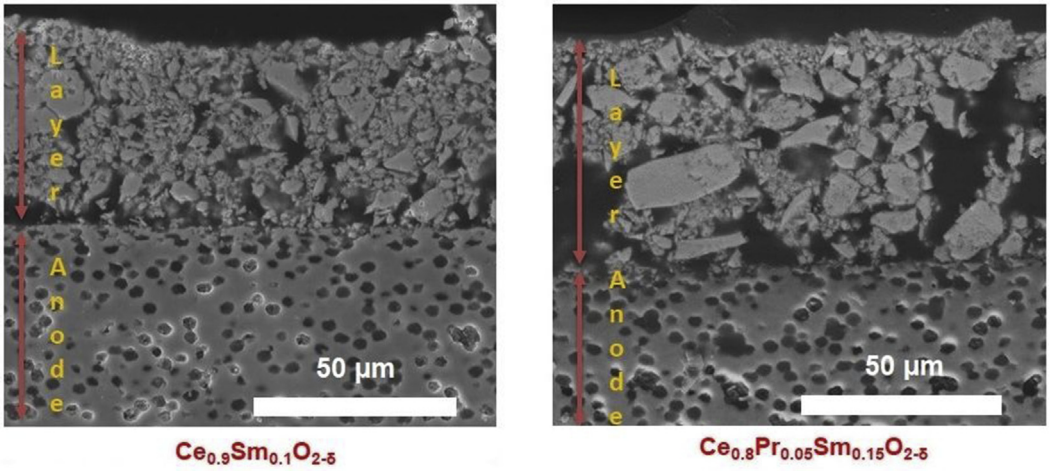

Fig. 5 – SEM images presenting $Ce_{0.9}Sm_{0.1}O_{2-\delta}$ and $Ce_{0.8}Pr_{0.05}Sm_{0.15}O_{2-\delta}$ catalytic layers deposited on the surface of NiO-YSZ anode after sintering at 1000 °C for 2 h.

reported in the literature for Pr-doped ceria compounds [9,10,29,30]. It is explained by a chemical strain originating from the combination of slight contraction of the unit cell upon formation of oxygen vacancies and expansion of the unit cell upon partial reduction of praseodymium from Pr^{4+} to Pr^{3+} (according to Eqs. (1) and (2)) [9,10]. Therefore, the quality of the interface between the NiO-YSZ anode and the Pr-containing ceria catalytic layer may be poor. In consequence, it may be less adherent to the substrate and thus be more prone to mechanical damage. However, this weaker interface should not affect the catalytic properties of the layer itself. As long as effective gas diffusion can occur in the layer, biogas reforming chemical reactions should be performed, regardless of contact with the support. In turn, electrocatalytic reactions will require good electrical contact between the NiO-YSZ substrate and the layer (to allow transport of O^{2-} ions), but even point contact enabling the formation of a percolation path should be sufficient and the layer will fulfil its role.

During operation in biogas

After the analysis of structural properties of the fabricated compounds and their compatibility with the NiO-YSZ anode support they were investigated as an additional anode catalytic layers in SOFCs fueled by biogas. The results of electrical measurements are presented as current density plots versus time in Fig. 7. The data were normalised to the standard value of 100% in the moment of fuel switching from hydrogen to biogas. Such a presentation allows us to exclude the effect of different gas diffusion through a layer due to a different microstructure, which may influence the absolute value of a power density. To make it possible to know the actual current density values at which the fuel cells operated, an I–V plot for the reference SOFC without a layer was added to Supplementary Materials (Fig. S4). In Fig. 7 one can see that after fuel switching from hydrogen to biogas a rapid drop of current density takes place. This is due to fuel dilution with CH_4 and CO_2 and low fuel utilisation factor in this experiment. Among

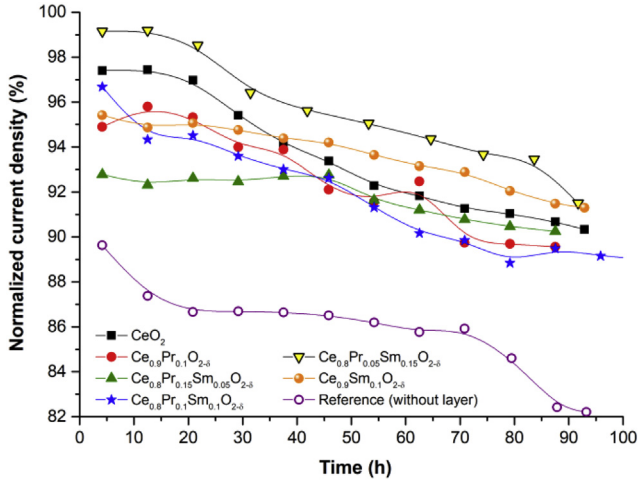

Fig. 7 – Normalised current density as a function of time in biogas atmosphere for SOFCs with additional Ce(Pr,Sm)$O_{2-\delta}$ catalytic layers and for a reference SOFC (without catalytic layer).

all investigated compounds the $Ce_{0.8}Pr_{0.05}Sm_{0.15}O_{2-\delta}$ layer seems to be the most resistant to fuel change whereas the $Ce_{0.8}Pr_{0.15}Sm_{0.05}O_{2-\delta}$ provides the biggest drop of current density after fuel switching. However, after the initial deterioration $Ce_{0.8}Pr_{0.05}Sm_{0.15}O_{2-\delta}$ ensures the best long-term stability, which was not observed for other investigated catalytic layers. For the rest of the presented layers further biogas feeding causes progressive degradation of the cell, which is responsible for a constant decrease in the current density (even up to 10% within 90 h of biogas feeding). Therefore one may state that none of these layers is a perfect catalyst for a direct internal reforming of biogas. However, comparing these results with the performance of a reference fuel cell (without a catalytic layer) in a similar experiment, then a beneficial effect of using the catalytic layer is clearly visible. All of the investigated layers give lower current density drop after hydrogen/biogas switching which may be explained by the ability of more effective direct internal reforming of biogas.

To better understand the direct internal reforming of biogas and its influence on SOFC performance it is necessary to analyze also the composition of the outlet gases from the fuel cell. All possible reactions occurring at the anode side are presented in Table 3. Among them, one can find three undesired processes: CH_4 pyrolysis (5), Boudouard reaction (6) and CO reduction (7) leading to a formation of a solid carbon, which can block the active area of the catalyst, impede the diffusion of fuel to the triple phase boundary (TPB) as well as it can even destroy the anode structure. The first reaction is an endothermic process, while the others are exothermic.

The results of the in situ FTIR analysis for the selected representative compositions: $Ce_{0.9}Pr_{0.1}O_{2-\delta}$ and $Ce_{0.9}Sm_{0.1}O_{2-\delta}$ (monodoped) and $Ce_{0.8}Pr_{0.1}Sm_{0.1}O_{2-\delta}$ (co-doped) are presented in Fig. 8 as time dependencies of concentration of the particular outlet gases and corresponding catalytic parameters: the conversion rates of CH_4 and CO_2, the CO and H_2 selectivities and the yields of CO and H_2. The results obtained for all investigated compounds are given in the Supplementary Materials (Figs. S1 and S2). A detailed description of how these parameters were calculated can be found in our previous paper [16].

The most stable in time composition of outlet gases were noticed for SOFC with the $Ce_{0.9}Sm_{0.1}O_{2-\delta}$ layer. The initial increase of CH_4 and CO_2 concentration is related to a dilution of initial synthetic biogas mixture (60% of CH_4 and 40% of CO_2) by the hydrogen remaining in the measuring rig as well as by the initial very intensive internal reforming performed in the whole volume of the catalyst. After a few hours of operation under biogas a kind of equilibrium state is reached. This stabilisation is visible also in corresponding catalytic parameters (Fig. 8 right): conversion rates of CH_4 and CO_2, the CO and H_2 selectivities and the yields of CO and H_2. Among two other presented catalysts the worst is $Ce_{0.9}Pr_{0.1}O_{2-\delta}$, regarding the lowest stability in time as well as the least effective internal reforming (the highest amount of unreacted fuel with simultaneous the lowest amount of products). The co-doped $Ce_{0.8}Pr_{0.1}Sm_{0.1}O_{2-\delta}$ composition is clearly between the other two compounds. It should be noted that additional beneficial effect of co-doping is visible in more detailed non-equilibrium chemical analysis, which was performed based on FTIR measurements. It allowed to determine a contribution and direction of the particular chemical reactions to the direct

Table 3 – Possible reactions (and their enthalpies) of direct internal reforming of biogas in DIR-SOFC [31–33].

(1)	Steam reforming of CH_4	$CH_4+H_2O \leftrightarrow CO+3H_2$	$\Delta H^0_{298} = 206\ kJmol^{-1}$
(2)	Dry reforming of CH_4	$CH_4+CO_2 \leftrightarrow 2CO+2H_2$	$\Delta H^0_{298} = 247\ kJmol^{-1}$
(3)	Reverse water-gas shift	$CO_2+H_2 \leftrightarrow CO + H_2O$	$\Delta H^0_{298} = 41\ kJmol^{-1}$
(4)	Methanation	$CO_2+4H_2 \leftrightarrow CH_4 + 2H_2O$	$\Delta H^0_{298} = -165\ kJmol^{-1}$
(5)	CH_4 pyrolysis (methane cracking)	$CH_4 \leftrightarrow C_{solid} + 2H_2$	$\Delta H^0_{298} = 75\ kJmol^{-1}$
(6)	CO disproportionation (Boudouard reaction)	$2CO \leftrightarrow C_{solid} + CO_2$	$\Delta H^0_{298} = -173\ kJmol^{-1}$
(7)	CO reduction	$CO + H_2 \leftrightarrow C_{solid} + H_2O$	$\Delta H^0_{298} = -131\ kJmol^{-1}$
(8)	Electrochemical oxidation of H_2	$H_2+O^{2-} \leftrightarrow H_2O + 2e^-$	$\Delta H^0_{298} = -242\ kJmol^{-1}$
(9)	Electrochemical oxidation of CO	$CO + O^{2-} \leftrightarrow CO_2 + 2e^-$	$\Delta H^0_{298} = -283\ kJmol^{-1}$
(10)	Electrochemical oxidation of CH_4	$CH_4+O^{2-} \leftrightarrow 2H_2 + CO + 2e^-$	$\Delta H^0_{298} = -37\ kJmol^{-1}$
(11)	Electrochemical oxidation of solid carbon	$C_{solid} + O^{2-} \leftrightarrow CO + 2e^-$	$\Delta H^0_{298} = -110\ kJmol^{-1}$

internal reforming process and to recognise which of them are mostly responsible for carbon deposition. A detailed description of the procedure was shown in our previous paper [16]. The results for $Ce_{0.8}Pr_{0.1}Sm_{0.1}O_{2-\delta}$ are shown in Fig. 9. Both time dependencies of reaction quotients (Q_r) for reactions (1)–(4) from Table 3 (Fig. 9 left) and carbon activity coefficients ($\alpha_{C,r}$) for reactions (5)–(7) from Table 3 (Fig. 9 right) are presented.

It is generally agreed that $Q_r \sim 10^{-3}$ stands for the situation when mostly reactants are present in reaction area, while $Q_r \sim 10^3$ when nearly all substances are products and finally if $10^{-3} < Q_r < 10^3$ then significant amounts of both reactants and products are visible [16,34]. Therefore, related to our results, steam reforming of methane (1) is a dominant reaction, most probably due to the existence of an observable amount of water in reaction atmosphere. Both dry reforming (2) and RWGS (3) oscillate around an equilibrium, what is in agreement with other literature reports [35]. In turn, methanation reaction (4) is fully shifted towards reactants and takes part in decomposition of CH_4 rather than its formation.

The next parameter, carbon activity coefficient ($\alpha_{C,r}$) should be equal to 1 at the equilibrium point. When $\alpha_{C,r} > 1$, then a solid carbon formation is promoted [36,37]. Based on our results it can be concluded that both Boudouard reaction (6) and CO reduction (7) are rather shifted towards reactants (are lower than unity) and do not lead to carbon deposition on the anode side. This is probably due to an addition of water into fuel stream and a formation of additional water molecules by electrochemical hydrogen oxidation (8), which promote rather carbon gasification than deposition. Only $\alpha_{C,r}$ for CH_4 pyrolysis is significantly higher than 1 over whole measurement time, which clearly indicates that this reaction is responsible for carbon accumulation in investigated SOFC.

This dominance of a steam reforming of methane (1) in a complex internal biogas reforming process as well as CH_4 pyrolysis (5) as a main reaction responsible for carbon deposition was also observed for all other investigated SOFCs with catalytic layers. The only difference between them is the dynamics of time changes of the Q_r and $\alpha_{C,r}$ parameters. Therefore time dependencies of Q_r for steam reforming and $\alpha_{C,r}$ for CH_4 pyrolysis were set in one graph for all samples and shown in Fig. 10. To better understand these graphs it should be explained that the rate of time changes of quotients' values can illustrate how far from equilibrium point is each of reactions at a given time. Indirectly, a course of plotted function can deliver an overall view on how efficiently different reactions are trying to reach their equilibrium points. The higher is the change of calculated Q_r in time, the bigger is the difference between the actual concentration of products and equilibrium composition [38]. On the other hand, the time changes of $\alpha_{C,r}$ parameter, that is a reciprocal of Q_r, should be understood in an opposite way. The more rapidly particular reactions responsible for coking move away from the equilibrium point, the lower might be the rates of these reactions, leading to slower carbon accumulation [38]. To prove it, additional plots of carbon balance in time can be drawn. This parameter is calculated as a difference between the numbers of moles of carbon in the inlet and the outlet stream of gases and gives us the information about an average rate of carbon deposition during dwell time. A comparison of time changes of carbon balance for all investigated SOFCs can be found in Fig. 11. The lower is the decrease in carbon balance over time, the more stable is the operation of an analysed fuel cell. A rapid drop of this parameter is an undesired phenomenon, as it may indicate that the reforming process has slowed down (most probably due to the carbon accumulation and/or a change in the microstructure of the catalyst).

Therefore, based on the data collected in Figs. 10 and 11 and explanation given upwards, it may be concluded that $Ce_{0.9}Sm_{0.1}O_{2-\delta}$ and $Ce_{0.8}Pr_{0.05}Sm_{0.15}O_{2-\delta}$ are the most attractive compounds towards steam reforming of methane, whereas $Ce_{0.8}Pr_{0.15}Sm_{0.05}O_{2-\delta}$ is the most stable in time for this reaction, but not so effective. The activity of $Ce_{0.9}Sm_{0.1}O_{2-\delta}$ and $Ce_{0.8}Pr_{0.05}Sm_{0.15}O_{2-\delta}$ leads to more efficient conversion of methane and production of CO/H_2, what is in agreement with a composition of outlet gases and catalytic parameters shown in Fig. 8. Moreover, in general, it also corresponds well with higher values of current density (Fig. 7) obtained for these fuel cells. However, current density depicts us an efficiency of fuel utilisation and the ability to perform electrochemical reactions in particular compounds, what may be (but it doesn't have to be) in agreement with concentration of outlet gases.

Regarding the carbon accumulation in particular catalytic layers, the $Ce_{0.9}Pr_{0.1}O_{2-\delta}$ is the least stable (the biggest decrease of carbon balance over time, see Fig. 11) while the carbon deposition due to CH_4 pyrolysis is the slowest (the biggest increase of $\alpha_{C,r}$ over time, see Fig. 10 right). However, the latter one goes also in pair with the slowest carbon removal indicated by a reverse direction of Boudouard reaction (6) and CO reduction (7). Finally, the SOFC with $Ce_{0.9}Pr_{0.1}O_{2-\delta}$ is very unstable in time, what corresponds well with the results of electrical measurements (Fig. 7). The

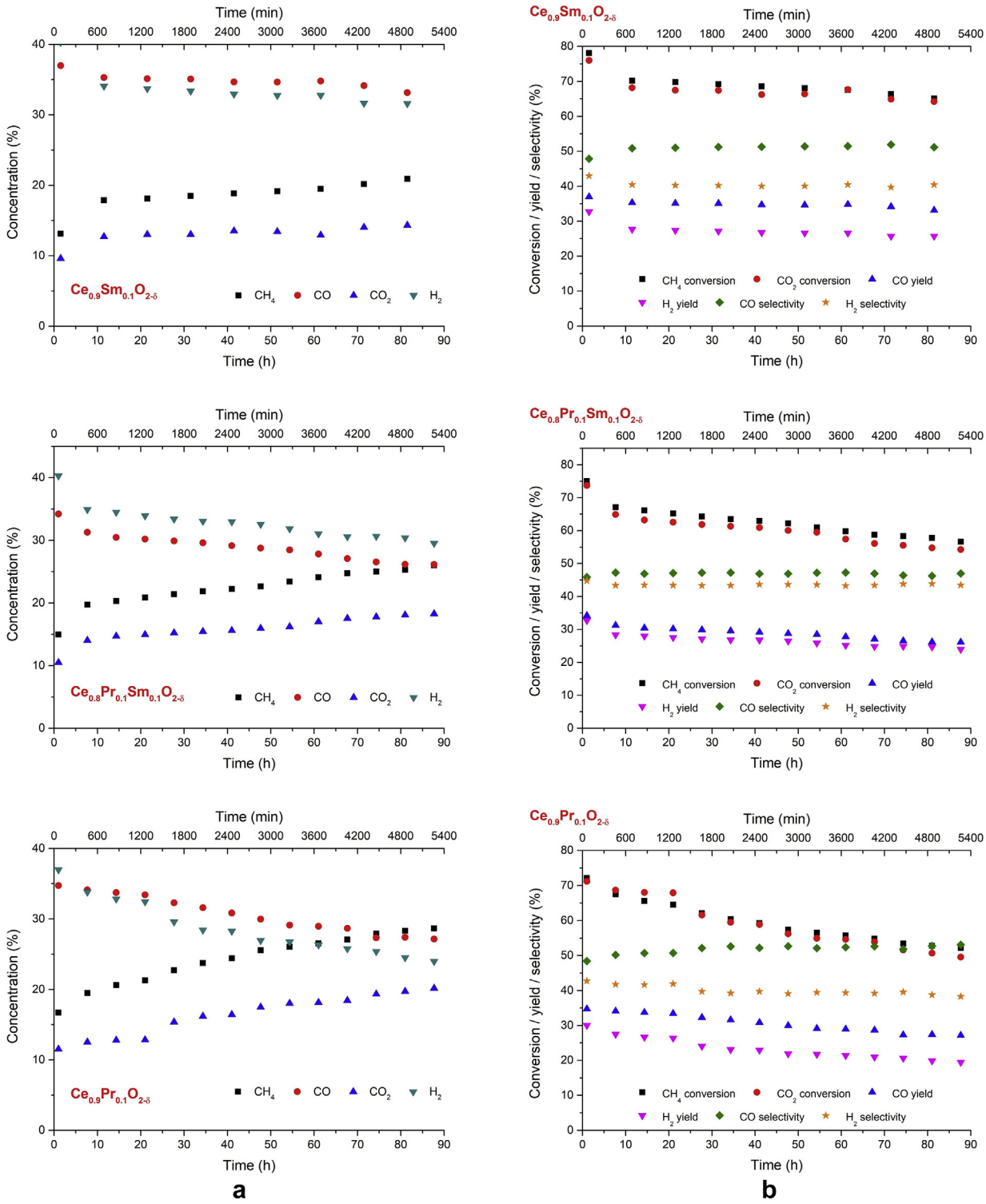

Fig. 8 – Plots presenting time dependencies of a) concentrations of outlet gases and b) CH_4, CO_2 conversion rates, CO and H_2 selectivities/yields for fuel cells with $Ce_{0.9}Sm_{0.1}O_{2-\delta}$, $Ce_{0.8}Pr_{0.1}Sm_{0.1}O_{2-\delta}$ and $Ce_{0.9}Pr_{0.1}O_{2-\delta}$ catalytic layers operating in a synthetic biogas.

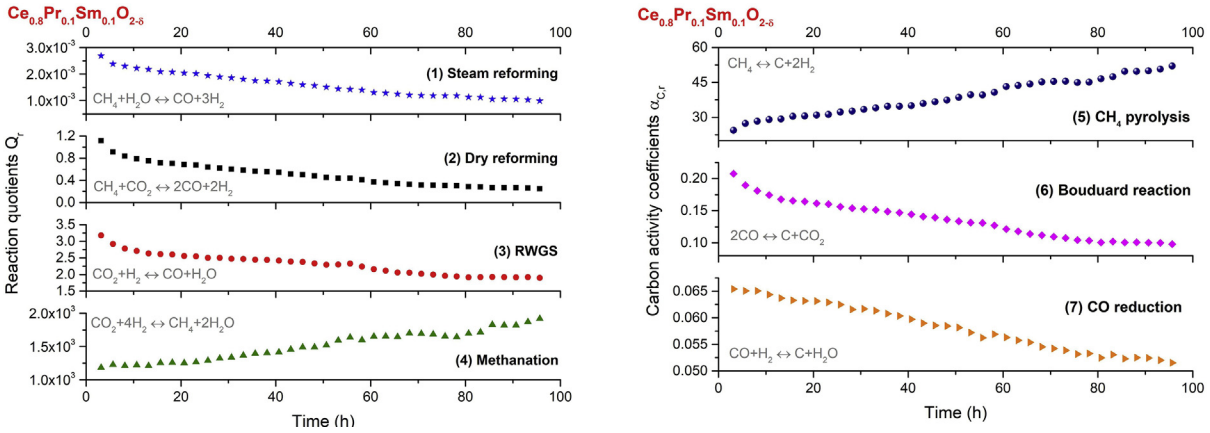

Fig. 9 – Left: Time dependence of reaction quotients (Q_r) for steam reforming (1), dry reforming (2), RWGS (3), methanation (4) reactions and right: Time dependence of carbon activity coefficients (α_c) for CH_4 pyrolysis (5), Boudouard reaction (6) and CO reduction (7) for a fuel cell with $Ce_{0.8}Pr_{0.1}Sm_{0.1}O_{2-\delta}$ catalytic layer.

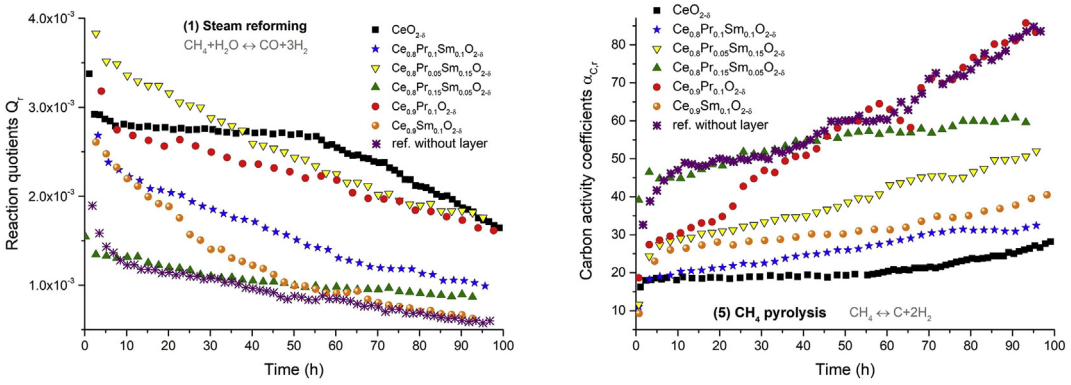

Fig. 10 – Time changes of: (left) reaction quotients (Q_r) for steam reforming (1) and (right) carbon activity coefficients (α_c) for CH_4 pyrolysis (5) for fuel cells with all investigated catalytic layers and without layer as a reference.

deterioration of its catalytic parameters is comparable with that observed for a reference fuel cell without any catalytic layer [16].

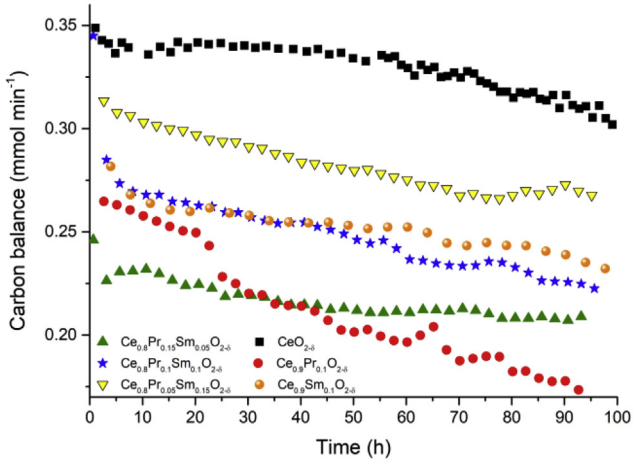

Fig. 11 – Time changes of carbon balance parameter for fuel cells with all investigated catalytic layers.

All these observations also allow to conclude that high praseodymium content in ceria-based compounds is not desirable. It does result in a slight improvement in catalytic properties, but undoubtedly it leads to the problems with TEC mismatch between the catalytic layer and NiO-YSZ support. In consequence, many cracks in the catalytic layer/anode interface occur, limiting the electrical contact between these constituents. Further, it deteriorates electrical properties of the operating SOFC, as well as limits electrochemical reactions leading to the oxidation of deposited solid carbon (reaction 11).

Finally, it is also worth to notice that in time dependence plots for all analysed parameters of $Ce_{0.9}Pr_{0.1}O_{2-\delta}$ compound there is a characteristic extremum point appearing at ~65 h of biogas feeding. At this point there is a local maximum of current density (Fig. 7), corresponding with a maximum of carbon balance (Fig. 11) and a minimum of carbon activity coefficient for CH_4 pyrolysis (Fig. 10 right). It correlates with a significant change in a fuel composition (Fig. 8), where unreacted methane starts to be a dominant component in an outlet stream of gases. Then, for a short time, a more intensive

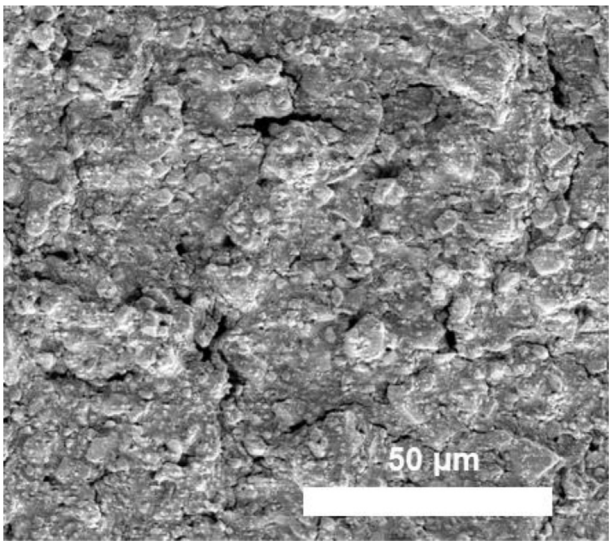

Fig. 12 – Post-mortem SEM image of $Ce_{0.9}Pr_{0.1}O_{2-\delta}$ layer after operation in biogas.

carbon accumulation takes place, giving a better electrical contact on the anode side and leading to higher current density. After 3–5 h a new equilibrium state is achieved and the internal biogas reforming further proceeds. The post-mortem SEM image of $Ce_{0.9}Pr_{0.1}O_{2-\delta}$ layer is shown in Fig. 12. It is uniform, with slight cracks randomly distributed. No visible traces of deposited carbon can be found, nor in the surface as well as in the cross section. This result is consistent and representative with other layers. It confirms, that although the investigated Pr and/or Sm doped ceria does not improve the DIR-SOFC electrical parameters, it protects from a significant deposition of a solid carbon, allowing SOFC to operate with biogas for a much longer time than without the additional layer. Even if a small amount of carbon is deposited at the end of the experiment, it seems to be very hard to determine its amount. Although the carbon balance (Fig. 11) could be integrated over time, it should be remembered that this is a dynamic measurement and depositing carbon is oxidised and removed from the cell on an ongoing basis. Only a structural form of possible carbon deposits could be determined using Raman spectroscopy [39,40] or Temperature Programmed Oxidation (TPO) [40–43]. However, for our layers, these methods did not give any reasonable results, as the amount of deposited carbon was too low.

Conclusions

The $CeO_{2-\delta}$, $Ce_{0.9}Sm_{0.1}O_{2-\delta}$, $Ce_{0.9}Pr_{0.1}O_{2-\delta}$, $Ce_{0.8}Pr_{0.15}Sm_{0.05}O_{2-\delta}$, $Ce_{0.8}Pr_{0.1}Sm_{0.1}O_{2-\delta}$ and $Ce_{0.8}Pr_{0.05}Sm_{0.15}O_{2-\delta}$ oxides, deposited in the form of layers on the surface of SOFC anode directly fed by biogas, were studied in aim to determine the influence of Pr and Sm on the fuel cell performance.

Regardless of the composition, the applied reverse microemulsion synthesis method allowed to obtain single-phase, nanocrystalline powders. It was found that in order to avoid the reaction between these oxides and the anode material (NiO-YSZ) sintering temperature should not exceed 1000 °C, since above that temperature a formation of the secondary $Ce_{1-x}Zr_xO_{2-\delta}$ phase was noticed.

It was also shown that Pr-doped ceria catalytic layers suffered from poor adhesion to the NiO-YSZ anode support due to a large mismatch in total thermal expansion coefficients of these materials. These observations are in agreement with previous literature reports. However, co-doping with Sm decreased the TEC significantly, leading to a better adhesion of the layer to the anode.

The studies of the influence of the catalytic layers on the direct internal reforming of biogas showed that Pr dopant deteriorates the properties of pure ceria. Single samarium doping or, if appropriate, an addition of a small amount of praseodymium is preferred. The $Ce_{0.9}Sm_{0.1}O_{2-\delta}$ and $Ce_{0.8}Pr_{0.05}Sm_{0.15}O_{2-\delta}$ materials are the most attractive towards steam reforming of methane, which is a dominant reaction among all processes occurring simultaneously in direct internal reforming of biogas. Their high activity led to more efficient conversion of methane and production of CO/H_2, what was in agreement with a composition of outlet gases and catalytic parameters. In turn, CH_4 pyrolysis was found to be a dominant reaction responsible for carbon accumulation on the anode side, but both carbon activity coefficient and carbon balance parameters confirmed that the $Ce_{0.9}Sm_{0.1}O_{2-\delta}$ and $Ce_{0.8}Pr_{0.05}Sm_{0.15}O_{2-\delta}$ show the highest stability over time and thus are the most attractive candidates for catalytic materials enhancing direct internal reforming of biogas in SOFC.

Declaration of competing interest

The authors declare that they have no known competing financial interests or personal relationships that could have appeared to influence the work reported in this paper.

Acknowledgements

This work was supported by the National Science Center under grant No. NCN 2017/26/D/ST8/00822.

Appendix A. Supplementary data

Supplementary data to this article can be found online at https://doi.org/10.1016/j.ijhydene.2020.07.146.

REFERENCES

[1] Escudero MJ, Fuerte A. Performance of ceria-electrolyte solid oxide fuel cell using simulated biogas mixtures as fuel. Adv Energy Power 2017;5(2):20–6. https://doi.org/10.13189/aep.2017.050202.

[2] Chaubey N, Wani BN, Bharadwaj SR, Chattopadhyaya MC. Physicochemical properties of rare earth doped ceria $Ce_{0.9}Ln_{0.1}O_{1.95}$ (Ln=Nd, Sm, Gd) as an electrolyte material for

IT-SOFC/SOEC. Solid State Sci 2013;20:135–41. https://doi.org/10.1016/j.solidstatesciences.2013.03.020.
[3] Da Silva AAA, Bion N, Epron F, Baraka S, Fonseca FC, Rabelo-Neto RC, Mattose LV, Noronha FB. Effect of the type of ceria dopant on the performance of Ni/CeO_2 SOFC anode for ethanol internal reforming. Appl Catal B Environ 2017;206:626–41. https://doi.org/10.1016/j.apcatb.2017.01.069.
[4] Balaguer M, Solís C, Serra JM. Structural–Transport properties relationships on $Ce_{1-x}Ln_xO_{2-\delta}$ system (Ln = Gd, La, Tb, Pr, Eu, Er, Yb, Nd) and effect of cobalt addition. J Phys Chem C 2012;116:7975–82. https://doi.org/10.1021/jp211594d.
[5] Fuerte A, Valenzuela RX, Escudero MJ. Role of dopants on ceria-based anodes for IT-SOFCs powered by hydrocarbon fuels. Univers J Electr Electron Eng 2017;5(3):45–55. https://doi.org/10.13189/ujeee.2017.050301.
[6] Tuller HL, Nowick AS. Small polaron electron-transport in reduced CeO_2 single-crystals. J Phys Chem Solid 1977;38:859–67. https://doi.org/10.1016/0022-3697(77)90124-X.
[7] Steele BCH. Appraisal of $Ce_{1-y}Gd_yO_{2-y/2}$ electrolytes for IT-SOFC operation at 500°C. Solid State Ionics 2000;129:95–110. https://doi.org/10.1016/S0167-2738(99)00319-7.
[8] Yahiro H, Eguchi K, Arai H. Electrical properties and reducibilities of ceria-rare earth oxide systems and their application to solid oxide fuel cell. Solid State Ionics 1989;36:71–5. https://doi.org/10.1016/0167-2738(89)90061-1.
[9] Cheng S, Chatzichristodoulou Ch, Søgaard M, Kaiser A, Hendriksen PV. Ionic/electronic conductivity, thermal/chemical expansion and oxygen permeation in Pr and Gd Co-doped ceria $Pr_xGd_{0.1}Ce_{0.9-x}O_{1.95-\delta}$. J Electrochem Soc 2017;164(13):F1354–67. https://doi.org/10.1149/2.0531713jes.
[10] Bishop SR, Tuller HL, Kuru Y, Yildiz B. Chemical expansion of nonstoichiometric $Pr_{0.1}Ce_{0.9}O_{2-\delta}$: correlation with defect equilibrium model. J Eur Ceram Soc 2011;31:2351–6. https://doi.org/10.1016/j.jeurceramsoc.2011.05.034.
[11] Zając W, Molenda J. Electrical conductivity of doubly doped ceria. Solid State Ionics 2008;179:154–8. https://doi.org/10.1016/j.ssi.2007.12.047.
[12] Andersson DA, Simak SI, Skorodumova NV, Abrikosov IA, Johansson B. Optimization of ionic conductivity in doped ceria. Proc Natl Acad Sci Unit States Am 2006;103:3518–21. https://doi.org/10.1073/pnas.0509537103.
[13] Coduri M, Checchia S, Longhi M, Ceresoli D, Scavini M. Rare earth doped ceria: the complex connection between structure and properties. Front Chem 2018;6:1–23. https://doi.org/10.3389/fchem.2018.00526.
[14] Bochentyn B, Chlipała M, Gazda M, Wang S-F, Jasiński P. Copper and cobalt co-doped ceria as an anode catalyst for DIR-SOFCs fueled by biogas. Solid State Ionics 2019;330:47–53. https://doi.org/10.1016/j.ssi.2018.12.007.
[15] Wyckoff RWG. Note: cadmium iodide structure. Crystal structures. 2nd ed., vol. 1. New York: Interscience Publishers; 1963. p. 239–444. https://doi.org/10.1107/S0365110X65000361.
[16] Chlipała M, Białk O, Wang S-W, Jasiński P, Bochentyn B. In situ study of a composition of outlet gases from biogas fuelled solid oxide fuel cell performed by the Fourier Transform Infrared Spectroscopy. Int J Hydrogen Energy 2019;44:13864–74. https://doi.org/10.1016/j.ijhydene.2019.03.243.
[17] Georges S, Bailly N, Steil C, Bultel Y, Hadjar A. SOFC long term operation in pure methane by gradual internal reforming. Electrochem soc 2013;57(1):3023–30. https://doi.org/10.1149/05701.3023ecst.
[18] van Biert L, Godjevac M, Visser K, Aravind PV. Dynamic modelling of a direct internal reforming solid oxide fuel cell stack based on single cell experiments. Appl Energy 2019;250:976–90. https://doi.org/10.1016/j.apenergy.2019.05.053.
[19] Yahiro H, Eguchi Y, Eguchi K, Arai H. Oxygen ion conductivity of the ceria-samarium oxide system with fluorite structure. J Appl Electrochem 1988;18:527–31. https://doi.org/10.1007/BF01022246.
[20] Shannon RD. Revised effective ionic radii and systematic studies of interatomic distances in halides and chalcogenides. Acta Crystallogr 1976;A32:751–67. https://doi.org/10.1107/S0567739476001551.
[21] Boaro M, Desinan S, Abate C, Ferluga M, De Leitenburg C, Trovarelli A. Study on redox, structural and electrical properties of $Ce_xZr_{1-x}O_2$ for applications in SOFC anodes. J Electrochem Soc 2011;158(2):P22–9. https://doi.org/10.1149/1.3518756.
[22] Di Monte R, Kaspar J. Nanostructured CeO_2-ZrO_2 mixed oxides. J Mater Chem 2005;15:633–48. https://doi.org/10.1039/B414244F.
[23] Boaro M, Trovarelli A, Hwang JH, Mason TO. Electrical and oxygen storage/release properties of nanocrystalline ceria–zirconia solid solutions. Solid State Ionics 2002;147:85–95. https://doi.org/10.1016/S0167-2738(02)00004-8.
[24] Patel S, Jawlik PF, Wang L, Jackson GS, Almansoori A. Impact of cofiring ceria in Ni/YSZ SOFC anodes for operation with syngas and n-butane. J Fuel Cell Sci Technol 2012;9(4):041002. https://doi.org/10.1115/1.4006823.
[25] Cimenti M, Alzate-Restrepo V, Hill JM. Direct utilisation of methanol on impregnated Ni/YSZ and Ni–$Zr_{0.35}Ce_{0.65}O_2$/YSZ anodes for solid oxide fuel cells. J Power Sources 2010;195:4002–12. https://doi.org/10.1016/j.jpowsour.2009.12.119.
[26] Wang W, Qu J, Julião PSB, Shao Z. Recent advances in the development of anode materials for solid oxide fuel cells utilizing liquid oxygenated hydrocarbon fuels: a mini review. Energy Technol 2019;7:33–44. https://doi.org/10.1002/ente.201700738.
[27] Pergolesi D, Gilardi E, Fabbri E, Roddatis V, Harrington GF, Lippert T, Kilner JA, Traversa E. Interface effects on the ionic conductivity of doped ceria - yttria-stabilized zirconia heterostructures. ACS Appl Mater Interfaces 2018;10(16):14160–9. https://doi.org/10.1021/acsami.8b01903.
[28] Basu S. Recent trends in fuel cell science and technology. New York: Springer; 2007.
[29] Chockalingam R, Ganguli AK, Basu S. Praseodymium and gadolinium doped ceria as a cathode material for low temperature solid oxide fuel cells. J Power Sources 2014;250:80–9. https://doi.org/10.1016/j.jpowsour.2013.10.105.
[30] Ftikos Ch, Nauer M, Steele BCH. Electrical conductivity and thermal expansion of ceria doped with Pr, Nb and Sn. J Eur Ceram Soc 1993;12:267–70. https://doi.org/10.1016/0955-2219(93)90101-V.
[31] Dang-Long T, Quang-Tuyen T, Shiratori Y. Catalytic and electrochemical behaviour of solid oxide fuel cell operated with simulated-biogas mixtures. AIP Conference Proceedings 2016;1737:060012. https://doi.org/10.1063/1.4949319.
[32] Shiratori Y, Ijichi T, Oshima T, Sasaki K. Internal reforming SOFC running on biogas. Int J Hydrogen Energy 2010;35:7905–12. https://doi.org/10.1016/j.ijhydene.2010.05.064.
[33] Iyer MV, Norcio LP, Kugler EL, Dadyburjor DB. Kinetic modeling for methane reforming with carbon dioxide over a mixed-metal carbide catalyst. Ind Eng Chem Res 2003;42:2712–21. https://doi.org/10.1021/ie020677q.
[34] Petrucci RH, et al. General chemistry principles & modern applications. 9th ed. Upper Saddle River, NJ: Pearson Prentice Hall; 2007. https://trove.nla.gov.au/work/9799296.

[35] Barroso Quiroga MM, Castro Luna AE. Kinetic analysis of rate data for dry reforming of methane. Ind Eng Chem Res 2007;46:5265–70. https://doi.org/10.1021/ie061645w.
[36] Jaworski Z, Zakrzewska B, Pianko-Oprych P. On thermodynamic equilibrium of carbon deposition from gaseous C-H-O mixtures: updating for nanotubes. Rev Chem Eng 2017;33:217–35. https://doi.org/10.1515/revce-2016-0022.
[37] Tsiakaras P, Demin A. Thermodynamic analysis of a solid oxide fuel cell system fuelled by ethanol. J Power Sources 2001;102:210–7. https://doi.org/10.1016/S0378-7753(01)00803-5.
[38] Hołówko B, Błaszczak P, Chlipała M, Gazda M, Wang S-F, Jasiński P, Bochentyn B. Structural and catalytic properties of ceria layers doped with transition metals for SOFCs fueled by biogas. Int J Hydrogen Energy 2020;45:12982–96. https://doi.org/10.1016/j.ijhydene.2020.02.144.
[39] Niu B, Jin F, Yang X, Feng T, He T. Resisting coking and sulfur poisoning of double perovskite Sr2TiFe0.5Mo0.5O6–δ anode material for solid oxide fuel cells. Int J Hydrogen Energy 2018;43:3280–90. https://doi.org/10.1016/j.ijhydene.2017.12.134.
[40] Moreira Sarruf BJ, Hong JE, Steinberger-Wilckens R, Valadão de Miranda PE. Ceria-Co-Cu-based SOFC anode for direct utilisation of methane or ethanol as fuels. Int J Hydrogen Energy 2020;45:5297–308. https://doi.org/10.1016/j.ijhydene.2019.04.075.
[41] Da Silva AAA, Bion N, Epron F, Baraka S, Fonseca FC, Rabelo-Neto RC, Mattose LV, Noronha FB. Effect of the type of ceria dopant on the performance of Ni/CeO_2 SOFC anode for ethanol internal reforming. Appl Catal B Environ 2017;206:626–41. https://doi.org/10.1016/j.apcatb.2017.01.069.
[42] Da Costa LOO, Da Silva AM, Noronha FB, Mattos LV. The study of the performance of Ni supported on gadolinium doped ceria SOFC anode on the steam reforming of ethanol. Int J Hydrogen Energy 2012;37:5930–9. https://doi.org/10.1016/j.ijhydene.2012.01.008.
[43] Fuerte A, Valenzuela RX, Escudero MJ, Daza L. Effect of cobalt incorporation in copper-ceria based anodes for hydrocarbon utilisation in Intermediate Temperature Solid Oxide Fuel Cells. J Power Sources 2011;196:4324–31. https://doi:10.1016/j.jpowsour.2010.12.053.